Energy &
Environment Nexus

Original Research

Open Access

https://doi.org/10.48130/een-0025-0005

Modulating lattice distortion of $NiO/MgAl_{2-x}Fe_xO_4$ for low-temperature methane decomposition with CO_2 reduction

Zhao Sun, Zong Chen and Zhiqiang Sun*

Received: 20 June 2025

Revised: 2 August 2025

Accepted: 15 August 2025

Published online: 30 September 2025

Abstract

Methane decomposition technology is regarded as a promising pathway for one-step H_2 generation but suppressed by carbon deposition and catalyst deactivation. To solve these problems, a series of $NiO/MgAl_{2-x}Fe_xO_4$ ($0.50 \leq x \leq 2.00$) catalysts were prepared for accomplishing low-temperature H_2 generation from catalytic methane dissociation and alleviating catalyst invalidation through a carbon dioxide reduction strategy. Results indicate that a methane conversion of 91.03% and a hydrogen concentration of 91.21 vol% were achieved at 650 °C using $NiO/MgAlFeO_4$. Long-term durability experiments were conducted under high-temperature and carbon-deposited conditions, and the $NiO/MgAlFeO_4$ material still had highly satisfactory activity and stability after 20 cycles. It is revealed that the lattice distortions of Fe-O and Al-O in $NiO/MgAl_{2-x}Fe_xO_4$ could be the dominant factor for boosted hydrogen generation from methane decomposition, synergistically promoting methane activation and dehydrogenation. These findings provide new implications for advanced catalyst design, which will substantially promote methane decomposition in a highly efficient manner.

Keywords: Catalytic methane decomposition, Low-temperature hydrogen production, Lattice distortion modulation, $NiO/MgAlFeO_4$, CO_2 reduction

Highlights

- Low-temperature methane decomposition with carbon dioxide reduction was proposed.
- The $NiO/MgAlFeO_4$ catalyst showed excellent catalytic activity and stability in CMD.
- 91.03% CH_4 conversion and 91.21 vol% H_2 concentration can be obtained at 650 °C.
- Lattice distortion of $MgAl_{2-x}Fe_xO_4$ dominates graphitization degree of deposited carbon.

* Correspondence: Zhiqiang Sun (zqsun@csu.edu.cn)

Full list of author information is available at the end of the article.

Graphical abstract

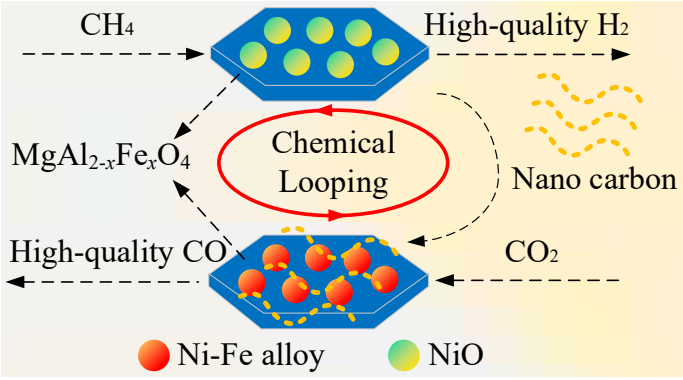

Introduction

Hydrogen, as a suitable substitute for fossil fuels, has attracted widespread attention owing to its renewable, clean, and carbon-free advantages[1,2]. Just as importantly, the calorific value of H_2 is 39.4 kWh/kg, about 2.75 times greater than that of other liquid hydrocarbon fuels[3,4]. Hydrogen production in an efficient and continuous manner is highly desired for the sustainable development of clean energy[5–7]. Relying on the abundant proven reserves worldwide, and the technological advantages of a high H/C ratio, natural gas is widely utilized for generating H_2[8–10]. Among methane-to-hydrogen production pathways, steam reforming of methane is a commercialized technology and a predominant industrial approach to producing hydrogen[11,12]. Nevertheless, the process suffers from complicated procedures, high energy consumption, and equipment costs. Moreover, carbon dioxide removal would also result in a substantial increase in the cost of producing hydrogen[13].

The decomposition of methane has garnered significant interest as a new route capable of generating hydrogen in one step. CO_x-free hydrogen could be theoretically produced by methane decomposition ($CH_4 \rightarrow C + 2H_2$), which is potentially used in Proton Exchange Membrane Fuel Cells (PEMFCs)[14,15]. Additionally, solid carbon material, the only byproduct, has a wide range of potential applications and economic value[16,17]. However, high temperatures > 1,200 °C are generally required to acquire reasonable hydrogen yields[18]. A significant reduction in decomposition temperature can be achieved by applying a catalyst, namely catalytic methane decomposition (CMD)[19]. Ni-based materials have been reported as promising candidates for CH_4 activation, due to their low cost and high activity[20,21]. Nevertheless, carbon deposition during CMD would result in the coverage of the active sites, thus lowering catalyst performance permanently[22–24].

Catalyst supports are especially crucial for enhancing active component dispersion and remaining catalyst stability[25]. $MgAl_2O_4$ is an excellent spinel material used as catalyst support for its high mechanical strength, thermal stability, and chemically inert properties[26,27]. Nuernberg et al.[28] prepared Ni/$MgAl_2O_4$ catalysts for methane decomposition using a wet impregnation method with methane conversion reaching up to 37% at 550 °C. They also verified that carbon nanotube can be effectively produced under the catalysis of Ni/$MgAl_2O_4$. Yu et al.[29] conducted the H_2-TPR measurements, and illustrated that the Ni/$MgAl_2O_4$ catalyst possesses a stronger metal-support interaction effect compared with Ni/MgO and Ni/γ-Al_2O_3, demonstrating high activity and superior sintering resistance in methane decomposition.

An alternate approach to enhancing the CMD performance involves the construction of bimetallic catalysts. The doping of noble metals [platinum (Pt)[30], ruthenium (Ru)[31], palladium (Pd)[32]] or transition metals (cobalt [Co][33], iron [Fe][34]) is reported to further promote the activity and the stability of Ni-based catalysts due to the structural and electronic rearrangements during alloy formation. The performance of Ni-Fe alloy-based catalysts has been reported and proven to be effective[35,36]. Chesnokov & Chichkan[37] performed the kinetic analysis regarding CMD reaction using Ni-Cu-Fe-based catalyst, and results demonstrated that the catalyst durability is strongly connected to the carbon growth and carbon diffusion. Compared to Ni^0, the diffusion coefficient of carbon atoms in Fe^0 is greater by three orders of magnitude, which allows faster diffusion of the carbon atoms through alloy particles. This can facilitate carbon transfer and offer prolonged stability[38]. Despite these positive studies, Ni-Fe catalysts still require further exploration to enhance its low-temperature catalytic activity as well as its resistance to sintering and agglomeration[39,40].

In this regard, we propose a strategy for strengthening low-temperature CMD via *in situ* Ni-Fe alloy formation by incorporating Fe into the magnesium aluminate lattice. Specifically, nickel catalysts supported by $MgAl_{2-x}Fe_xO_4$ spinel were synthesized. On one hand, methane dissociation coupled with carbon dioxide reduction was conducted with the aim of resolving carbon deposition and catalyst deactivation; besides, the effects of FeO_6 and AlO_6 octahedral distortion on the CMD performances were explored with the aim of guiding the design of catalysts.

Materials and methods

Material preparation

$MgAl_{2-x}Fe_xO_4$ (x = 0.50, 0.75, 1.00, 1.25, 1.50, 1.75, 2.00) supports were prepared using a citric acid-induced sol-gel method as described previously[41]. $Mg(NO_3)_2{\cdot}6H_2O$, $Fe(NO_3)_3{\cdot}9H_2O$, $Al(NO_3)_3{\cdot}9H_2O$, and $Ni(NO_3)_2{\cdot}6H_2O$ were purchased from Sinopharm. Citric acid ($C_6H_6O_7$) was used as received from Aladdin. Typically, suitable metal nitrates, $Mg(NO_3)_2{\cdot}6H_2O$, $Al(NO_3)_3{\cdot}9H_2O$, and $Fe(NO_3)_3{\cdot}9H_2O$, were added into the deionized water according to the magnesium (Mg) : aluminium (Al) : Fe ratio of 1:(2-x):x ($0.50 \leq x \leq 2.00$). Citric acid was introduced as a complexing agent, maintaining a molar ratio of 1.3:1.0 between citric acid and total metal ions. The obtained solution was stirred at 80 °C in a water bath to a viscous state. The gel was dried at 150 °C for 12 h, and placed in a muffle furnace and calcined at 850 °C for 4 h under 2 °C/min. For synthesizing NiO/$MgAl_{2-x}Fe_xO_4$ catalysts, an aqueous solution of nickel nitrate hexahydrate was introduced into a suitable

amount of the prepared supports by incipient wetness impregnation with a NiO loading of 12 wt%[42,43]. Seven NiO/$MgAl_{2-x}Fe_xO_4$ catalysts, x = 0.50, 0.75, 1.00, 1.25, 1.50, 1.75, and 2.00, were denoted as S1–S7 (Supplementary Table S1).

Catalyst characterizations

The metal concentrations in the fresh catalysts were determined using ICP-OES (PerkinElmer Avio500).

The phase composition of the catalysts was examined by X-ray diffraction (XRD) using Cu Kα radiation (λ = 1.5406 Å) at 40 kV and 40 mA. Diffraction data were collected over a 2θ range of 10–90° with a scan rate of 7°/min and an increment of 0.02°.

Nitrogen adsorption-desorption experiments were carried out at −196 °C to determine the specific surface areas and pore structural parameters of the catalysts. Prior to measurement, all samples were degassed at 200 °C for 6 h under vacuum. The BET method was applied to calculate surface areas, while the BJH approach was used to derive pore size distribution and total pore volume.

The redox properties of the samples were investigated by H_2 temperature-programmed reduction (H_2-TPR) using a Micromeritics AutoChem II 2920 instrument. In a typical procedure, 100 mg of sample was loaded into a quartz reactor, pretreated at 300 °C under an Ar flow for 30 min, and then cooled to 50 °C for 1 h. Once the baseline stabilized, the temperature was raised from 50 to 1,000 °C at a heating rate of 10 °C/min in a flow of 10 vol% H_2/Ar (40 mL/min). H_2 consumption was monitored using a thermal conductivity detector (TCD).

Transmission electron microscopy (TEM, G2 60–300) was used to observe the morphology of fresh and spent catalysts. Elemental mapping for nickel (Ni), magnesium (Mg), Al, Fe, and oxygen (O) was performed via energy-dispersive X-ray spectroscopy (EDS). Prior to imaging, all samples were dispersed in ethanol and sonicated for 30 min.

Raman spectroscopy (Renishaw inVia) was conducted to probe carbon-related features, with measurements repeated at least three times per sample. Spectra were collected using a 532 nm laser, 10 s acquisition time, and a scan range of 40–4,000/cm.

X-ray photoelectron spectroscopy (XPS) was employed to determine the surface chemical states of both fresh and used NiO/$MgAlFeO_4$ catalysts. The measurements were conducted on a Thermo Scientific ESCALAB 250 system with a monochromatic Al Kα source (hv = 1,486.6 eV). Binding energies were calibrated using the C 1*s* peak at 284.8 eV as the internal standard.

Catalytic test

The catalytic activity experiments of the samples were carried out by a fixed-bed reactor (ID = 8 mm, length = 600 mm). Typically, a 0.400 g sample was placed at the center of the quartz reactor. Before the methane decomposition experiments, the reactor was flushed with 50 mL/min N_2 for 20 min. Then, the reactor was heated to 600, 650, 700, 750, or 800 °C at 10 °C/min. Once the temperature was stabilized, the gas was switched to a 10 vol% CH_4-N_2 steam (N_2 = 45 mL/min) with a duration time of 10~40 min. Similarly, the reactor was flushed by 50 mL/min N_2 for 20 min before the carbon dioxide reduction experiment. The carbon dioxide reduction test was performed for 60 min under the atmosphere of 10 vol% CO_2-N_2 stream (N_2 = 45 mL/min) within 750–900 °C. The protocol for the cyclic experiment was established as CH_4 decomposition for 40 min (50 mL/min 10 vol% CH_4-N_2) → N_2 purge for 10 min (50 mL/min N_2) → carbon dioxide reduction for 50 min (50 mL/min 20 vol% CO_2-N_2) → N_2 purge for 10 min (50 mL/min N_2). The outlet gas mixture was detected by an INFICON Micro GC equipped.

Data analysis

The gas productivity (mmol/min), the outlet flow rate of gas i (mmol/min), CH_4 conversion (%), and CO_2 conversion (%) were calculated as follows:

$$Y_{\text{total}} = \frac{Y(\text{N}_2,\text{out})}{C(\text{N}_2,\text{out})} \quad (1)$$

$$Y(i,\text{out}) = Y_{\text{total}} \cdot C(i,\text{out}) \quad (2)$$

$$X(\text{CH}_4) = \frac{Y(\text{CH}_4,\text{in}) - Y(\text{CH}_4,\text{out})}{Y(\text{CH}_4,\text{in})} \times 100\% \quad (3)$$

$$X(\text{CO}_2) = \frac{Y(\text{CO}_2,\text{in}) - Y(\text{CO}_2,\text{out})}{Y(\text{CO}_2,\text{in})} \times 100\% \quad (4)$$

where, Y_{total} denotes the total gaseous production rate; $Y(i, \text{in})$ and $Y(i, \text{out})$ represent the feeding rates of gas i and the production rate of gas i, respectively; $C(i, \text{out})$ is the concentration of generated gas i (i = N_2, CH_4, H_2, CO, or CO_2). $X(CH_4)$ and $X(CO_2)$ signify the methane and carbon dioxide conversion, respectively.

Results and discussion

Fresh catalyst characterization

ICP-OES results indicated that the Fe content in the catalyst increased while the Al content decreased with the Fe doping amounts, which aligns with the theoretical ratios (Supplementary Table S2). XRD results are displayed in Fig. 1, aiming at clarifying the phase of the fresh NiO/$MgAl_{2-x}Fe_xO_4$ catalysts. The diffractions of $MgAl_2O_4$ were mainly located at 19.0°, 31.3°, 36.9°, 44.8°, 55.7°, 59.4°, and 65.2° (JCPDS 99-0098). All the fresh catalysts with different Fe doping ratios showed diffraction peaks around these angles without the detection of other impurities, preliminarily confirming the formation of $MgAl_{2-x}Fe_xO_4$ after Fe incorporation. With the increase in the Fe doping amount, the peaks shifted to lower angles, attributing to lattice tensile strain caused by the substitution of Fe^{3+} (0.064,5 nm) by Al^{3+} (0.053,5 nm) in the spinel structure. Furthermore, three diffraction peaks (37.2°, 43.3°, and 62.9°) detected indicate the formation of NiO. The crystallite sizes of NiO were analyzed based on the Scherrer formula (Table 1). It is revealed that appropriate Fe doping is beneficial to maintain the small crystalline size of NiO. However, excessively high Fe doping results in an increase in the NiO crystalline size. In this regard, S3 and S4 catalysts are speculated to perform higher catalytic activity and stability during methane dissociation.

Textural properties of the fresh catalysts are presented in Table 1. The S1 sample possesses the largest BET surface area and pore volume, while a gradual decrease could be observed in surface area and pore volume with the further increase in the Fe doping amount[44,45].

The H_2-TPR results of the fresh samples are presented in Fig. 2. Support reduction followed the procedures of $MgFe^{III}AlO_4 \rightarrow Mg_{1-x}Fe^{II}_xO \rightarrow Fe^0$, which requires the complete separation of Fe with Mg and Al elements. Therefore, the presence of Al^{3+} and Mg^{2+} to some extent hinders the reduction of Fe^{3+}[46]. For the catalysts S1 to S4, the reduction peak located at ~430 °C corresponds to the reduction of surface amorphous NiO, indicating relatively weak interaction with the support. The main reduction peaks located at higher temperatures were assigned to the reduction of the NiO with a strong NiO-$MgAl_{2-x}Fe_xO_4$ interaction. Additionally, improving the Fe doping amount (S1 → S4), the peak shifted to high-temperature range, also confirming the increase in the interactions between NiO and $MgAl_{2-x}Fe_xO_4$. The strong interaction leads to the decrease of NiO crystallite size, which is consistent with XRD findings. With further increase in the Fe doping (1.25 ≤ x ≤ 2.00), two hydrogen reduction peaks obviously appeared for S5–S7 samples. The

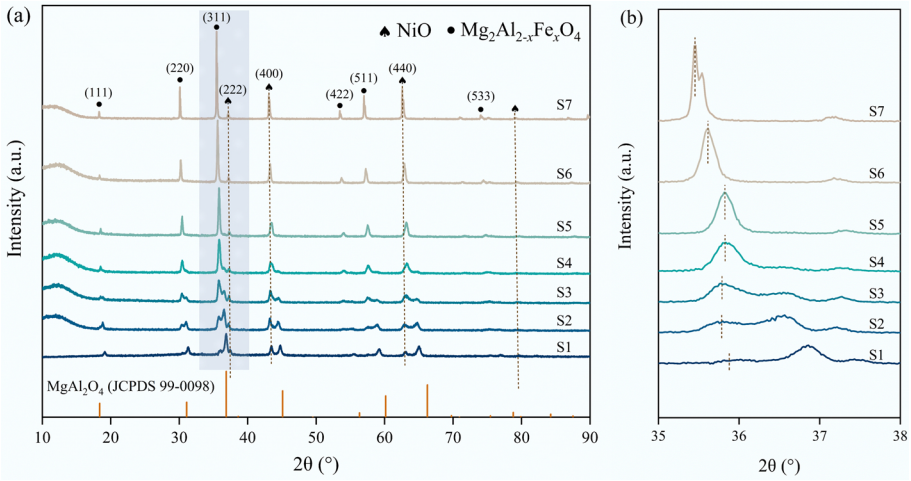

Fig. 1 XRD patterns of (**a**) fresh NiO/$MgAl_{2-x}Fe_xO_4$ (S1–S7); (**b**) local magnified XRD patterns.

reduction peak located within the lower temperature range corresponded to NiO → Ni, while the peak at a higher temperature was attributed to the reduction of the $MgAl_{2-x}Fe_xO_4$. Excessively high Fe doping promotes lattice oxygen mobility, resulting in the reduction peak shift towards lower temperatures.

The chemical states of fresh S1, S3, and S7 samples were further explored by XPS, as shown in Fig. 3 and Table 2. From Fig. 3a, Fe 2*p* spectra of S1, S3, and S7 were deconvoluted into four characteristic sub-peaks. For S3, the strong peak at 711.6 eV was assigned to Fe $2p_{3/2}$, and the peak at 724.9 eV was attributed to Fe $2p_{1/2}$, which are assigned to Fe^{3+}[47]. The Ni 2*p* spectra of S1, S3, and S7 samples are illustrated in Fig. 3b. The three catalysts exhibited a Ni $2p_{3/2}$ peak at 855.9 eV and a Ni $2p_{1/2}$ peak at 873.5 eV, indicating the existence of Ni^{2+}, which aligns with the XRD results. O 1*s* spectra of fresh S1, S3, and S7 catalysts are shown in Fig. 3c, in which the peaks were deconvoluted into three peaks OI (529.8 eV), OII (531.2 eV), and OIII (532.3 eV), corresponding to lattice oxygen, oxygen vacancy, and surface –OH species in the catalyst respectivel[48]. The ratio of lattice oxygen to oxygen vacancy (OI/OII) in these three catalysts increased with Fe doping amounts, confirming that Fe doping contributes to the formation of lattice oxygen (Table 2).

Catalytic methane decomposition

The CMD activities of the seven samples were firstly examined at 750 °C (Fig. 4). At the initial period of CMD, S1 to S5 samples exhibited satisfactory CH_4 conversion but relatively low H_2 concentration and H_2 yield, which can be ascribed to methane selective oxidation induced by the lattice oxygen. CH_4 conversion, H_2 concentration, and H_2 yield all increase as a function of CMD times. This can be attributed to Ni-Fe alloy formation, thus enhancing the catalytic performance, as proven by XRD (Supplementary Fig. S1).

Table 1 Textural properties of the fresh catalysts

Sample	BET surface area (m^2/g)	Pore volume (cm^3/g)	Average pore diameter (nm)	NiO crystallite size (nm)
S1	4.7	0.016	7.9	27.0
S2	3.6	0.012	5.0	20.3
S3	2.4	0.011	12.5	17.1
S4	3.4	0.016	12.6	16.0
S5	2.8	0.013	3.9	22.9
S6	2.3	0.010	3.5	34.1
S7	1.8	0.004	3.2	44.0

As shown in Fig. 4a and b, S1–S5 samples reached high H_2 concentrations as a function of time, while S6 and S7 samples exhibited inferior performance, indicating that a certain amount of Al doping is essential. Of the S1–S5 samples, S3 catalyst showed the best CMD activity and hydrogen evolution rate, and the H_2 concentration and the CH_4 conversion reached 97 vol% and 100%, respectively, after 40 min CMD (Fig. 4b and d). The gas concentration evolutions with CMD times by using S1, S2, S4, S5, and S6 catalysts are provided in Supplementary Fig. S2. After comprehensively considering CH_4 conversion, H_2 yield, and quality, the S3 sample was selected as the optimal catalyst for further exploration.

Raman measurements were carried out to identify graphitization degree of carbon on the spent S1–S7 catalysts after CMD (Fig. 5). Three peaks were observed at 1,335–1,348/cm, 1,565–1,580/cm, and 2,670–2,695/cm, corresponding to D, G, and 2D bands, respectively. D band represents disordered structures, which is ascribed to the vibration of the sp^3-hybridized carbon atom[49]. The G band is due to the in-plane vibrations of the sp^2-bonded carbon in ordered

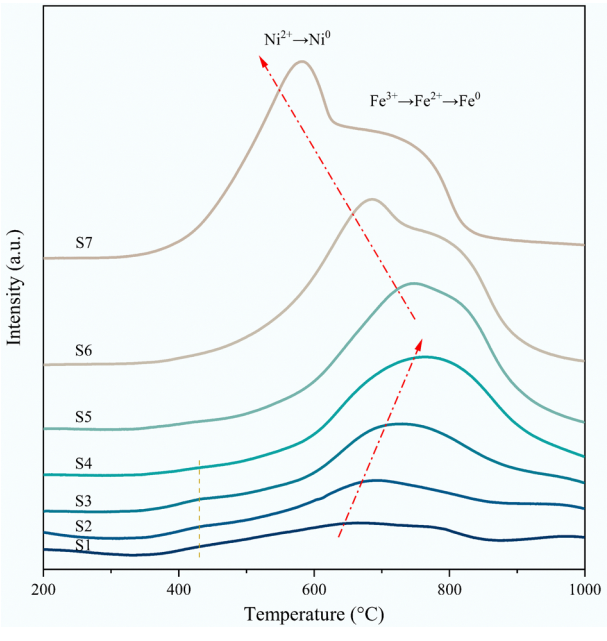

Fig. 2 H_2-TPR profiles of as-synthesized NiO/$MgAl_{2-x}Fe_xO_4$ samples.

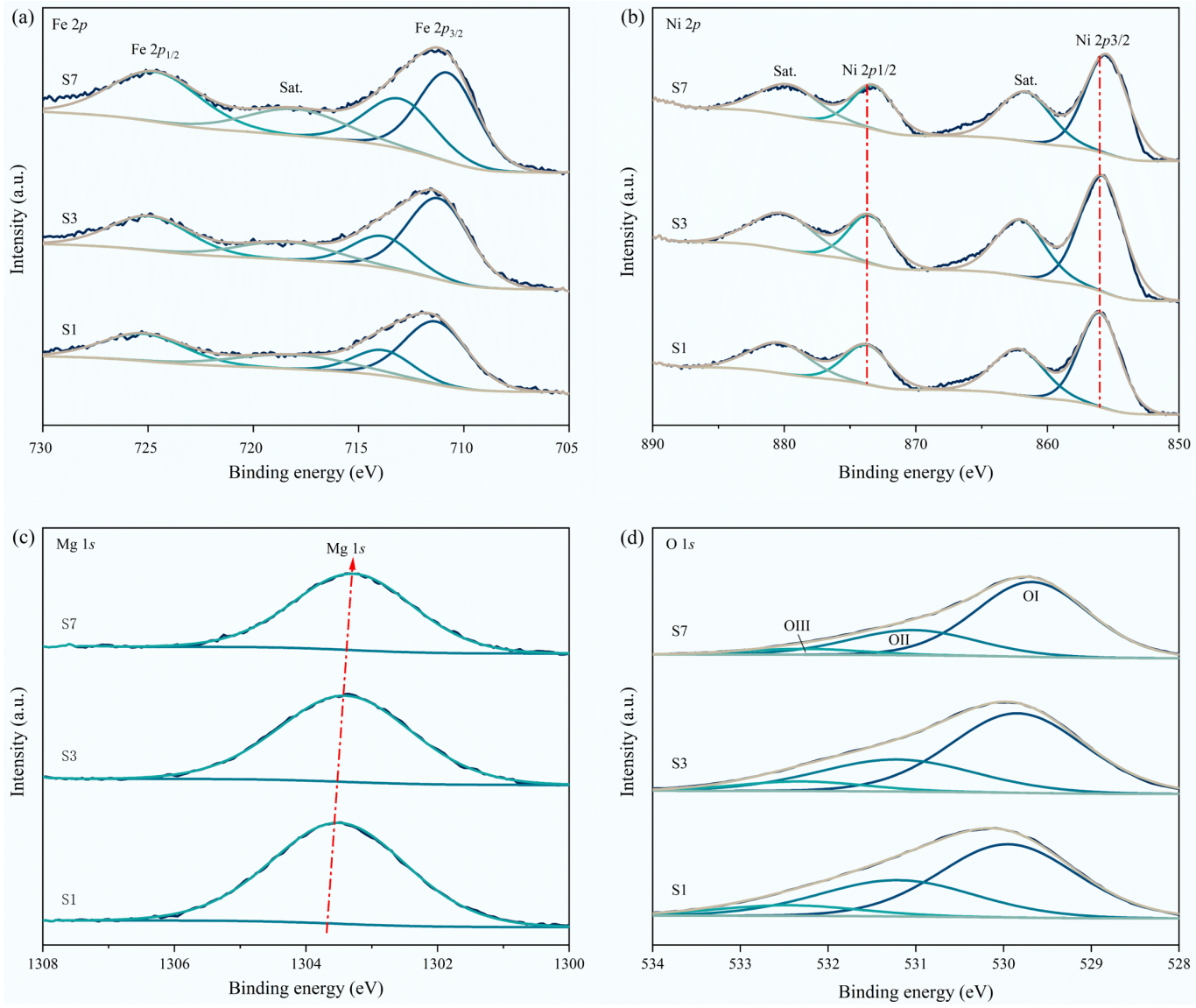

Fig. 3 XPS analysis of fresh S1, S3, and S7 catalysts. (**a**) Fe 2*p*; (**b**) Ni 2*p*; (**c**) Mg 1*s*, and (**d**) O 1*s*.

graphite[50,51]. 2D band is the second order of the D band[50]. The intensity ratio of the D band to G band (I_D/I_G) is related to the crystallinity and graphitization degree of the carbon species. Carbons with a high I_D/I_G ratios could favor their oxidation at lower temperatures[42,52]. Overall, except for the S7 sample, the carbon obtained from the carbon deposition in other samples had a relatively high degree of graphitization. Additionally, the graphitization degree of carbon exhibited a first decreasing and then increasing trend with the Fe content, and the carbon catalyzed by the S3 catalyst showed the highest I_D/I_G value.

Table 2 Summary of XPS characteristics of S1, S3, and S7 catalysts

Catalyst	Binding energy (eV)				Ratio			OI/OII
	Ni $2p_{3/2}$	Mg 1*s*	Al 2*p*	Fe $2p_{3/2}$	OI	OII	OIII	
S1	856.0	1303.5	74.2	711.3	0.58	0.33	0.09	1.76
S3	855.8	1303.4	73.9	711.2	0.63	0.30	0.07	2.10
S7	855.5	1303.3	/	710.7	0.68	0.26	0.05	2.62

Effect of CMD temperatures

CMD temperature shows significant effects on the methane decomposition performance. It can be observed from Fig. 6a, b, and c that the H_2 concentration CH_4 conversion, and H_2 yield show a gradually increasing tendency with methane decomposition temperatures, which is because of the acceleration of the C-H bond cleavage (Supplementary Fig. S3). Specifically, the H_2 concentration and CH_4 conversion with applied S3 catalyst reached 91.21 vol% and 91.03% at 650 °C, respectively, which implies the significant superiority of the S3 sample in low-temperature hydrogen generation from CMD. The hydrogen concentration and methane conversion reached up to 95.73 vol% and 97.82%, when the CMD temperature was raised to 700 °C (Fig. 6b and d). The NiO/$MgAlFeO_4$ (S3) catalyst also demonstrated higher CMD activity compared with other reported studies under nickel-based catalysts, and 700 °C was considered an appropriate temperature for methane decomposition (Supplementary Fig. S4)[34,49,53–55].

For a fresh S3 catalyst, NiO and $MgAlFeO_4$ are the main phases. After CMD, Ni-Fe alloy and $MgAl_{0.6}Fe_{1.4}O_4$ were observed as the

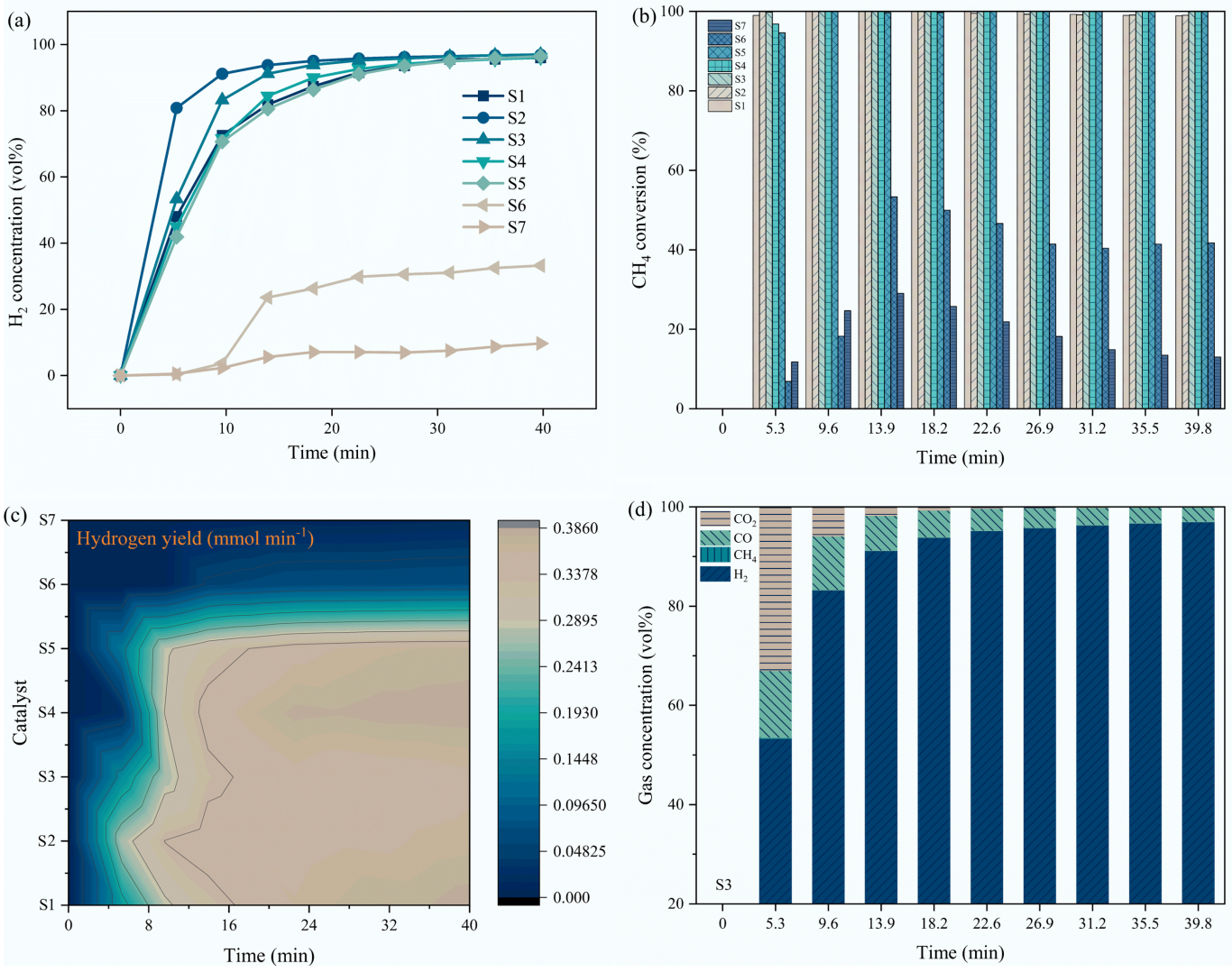

Fig. 4 Effect of Fe doping on the (**a**) H_2 concentration; (**b**) CH_4 conversion; (**c**) H_2 yield; (**d**) gas concentration of H_2, CH_4, CO, CO_2 under the catalysis of S3 catalyst.

main phases, indicating the occurrence of reduction and phase recombination of the catalyst. Specifically, the diffraction peaks appeared at smaller angles relative to metallic Ni, suggesting that Fe gradually migrated from support to surface with the formation of Ni-Fe alloy, as also described previously[56–58]. In addition, the characteristic peak of graphitic carbon was observed around 26.5° (JCPDS 02-0405), which is the product of methane decomposition.

To further clarify the intrinsic reason for highly efficient CMD, we calculated the lattice distortion of these catalysts under various Fe doping amounts. Zhang et al.[59] previously quantified the lattice distortion degree of the Ce modified $LaFeO_3$ perovskite by the method reported by Shannon[60,61]. The lattice distortion was carried out to evaluate the degree to which the Fe-O bond deviates from the average one. The lattice distortion of $MgAl_{2-x}Fe_xO_4$ supports, Δ(Fe-O) and Δ(Al-O), were assessed by the following equation:

$$\Delta = \frac{1}{6}\sum\left(\frac{R_i - R_{av}}{R_{av}}\right)^2 \quad (5)$$

where, R_{av} is the average bond length of the Fe-O or Al-O bond in the octahedron, and R_i is the actual bond length of each Fe-O or Al-O bond. Based on the above equation, the configurated structure of $MgAl_{2-x}Fe_xO_4$ support, as well as the relationship between the Fe doping amount x ($0.50 \le x \le 2.00$) and the lattice distortion degree of Fe-O and Al-O bonds, are shown in Fig. 7.

It can be found that the FeO_6 and AlO_6 distortion occurs with varying Fe doping amounts. On the one hand, Fe doping amounts of 0.75, 1.00, 1.25, and 1.50 performed high Fe-O distortions, which promotes the breaking of Fe-O bonds, thereby enhancing the formation of Ni-Fe alloy; on the other hand, Fe doping amounts under 0.50, 0.75, and 1.00 performed high Al-O distortions. This may alter the electron cloud distribution around Al^{3+}, enhancing its Lewis acidity and altering its electron density around the active Ni species, thereby facilitating methane dehydrogenation. According to the discussion above, the S2 and S3 samples were considered as promising catalysts, which is in full agreement with the experimental results, demonstrating synergistic lattice distortions of Fe-O and Al-O octahetral in boosting CMD activity.

The carbon graphitization degree after 40 min CMD at 600–800 °C was analyzed by Raman spectra (Fig. 8a). Three peaks in the D, G, and 2D bands of the deposited carbon can be observed. The I_D/I_G gradually decreased with the CMD temperatures, implying the gradually decreased carbon disorder degree. It is determined that a high temperature promotes generating highly graphitized carbon with

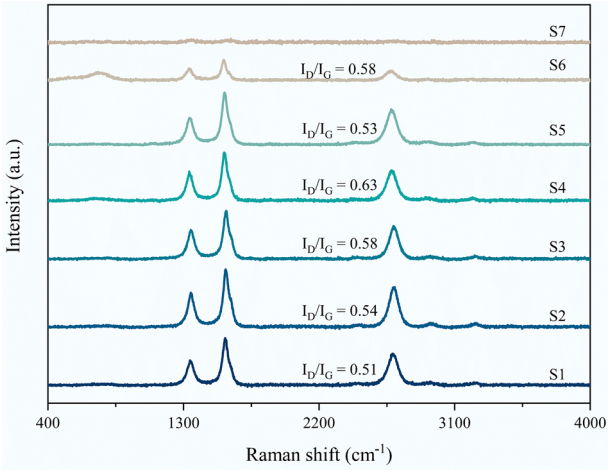

Fig. 5 Raman spectra of spent S1–S7 samples after 40 min CMD at 750 °C.

an ordered structure. The effect of CMD times from 10 to 40 min on the carbon graphitization degree was also studied at 700 °C. Figure 8b displays the positive correlation between the carbon graphitization degree and the CMD time, i.e., extending the CMD time can enhance its graphitization degree.

Effect of carbon dioxide reduction temperatures

Catalyst and carbon separation presents a significant challenge for gas-solid CMD technology. CO_2 is a commonly utilized gasification agent and thus was selected for eliminating the deposited carbon from CMD. The effect of carbon dioxide reduction temperatures from 750 °C to 900 °C on the carbon elimination performance was investigated (Fig. 9). As we expected, the increase in the carbon dioxide reduction temperature showed a positive impact on the carbon dioxide reduction, owing to higher C=O bond dissociation rate at high temperatures. According to the XRD results of the oxidized S3 sample, the cycled catalyst is mainly composed of Ni and $MgFeAlO_4$, while other phases such as $MgFe_{0.6}Al_{1.4}O_4$ and $(MgO)_{0.91}(FeO)_{0.09}$ were also detected. This confirmed that the main evolution of the S3 catalyst is: $NiO{\cdot}MgFeAlO_4 \rightarrow$ Ni-Fe alloy + $MgFe_{0.6}Al_{1.4}O_4 \rightarrow$ Ni + $MgFeAlO_4$, and Ni + $MgFeAlO_4$ would be a stable form of the cycled catalyst.

Stability test

Twenty cycles of methane decomposition (800°C) with carbon dioxide reduction (900 °C) were performed to explore the stability of the S3 catalyst (Fig. 10a–c). S3 sample showed remarkable catalytic activity and stability even after 20th cyclic experiments. The maximum concentration of H_2 dropped slightly from 97.95 vol% (1st cycle) to 95.27 vol% (20th cycle), and the concentrations of CO remained at approximately 97.00 vol%. The preeminent stability of the catalyst

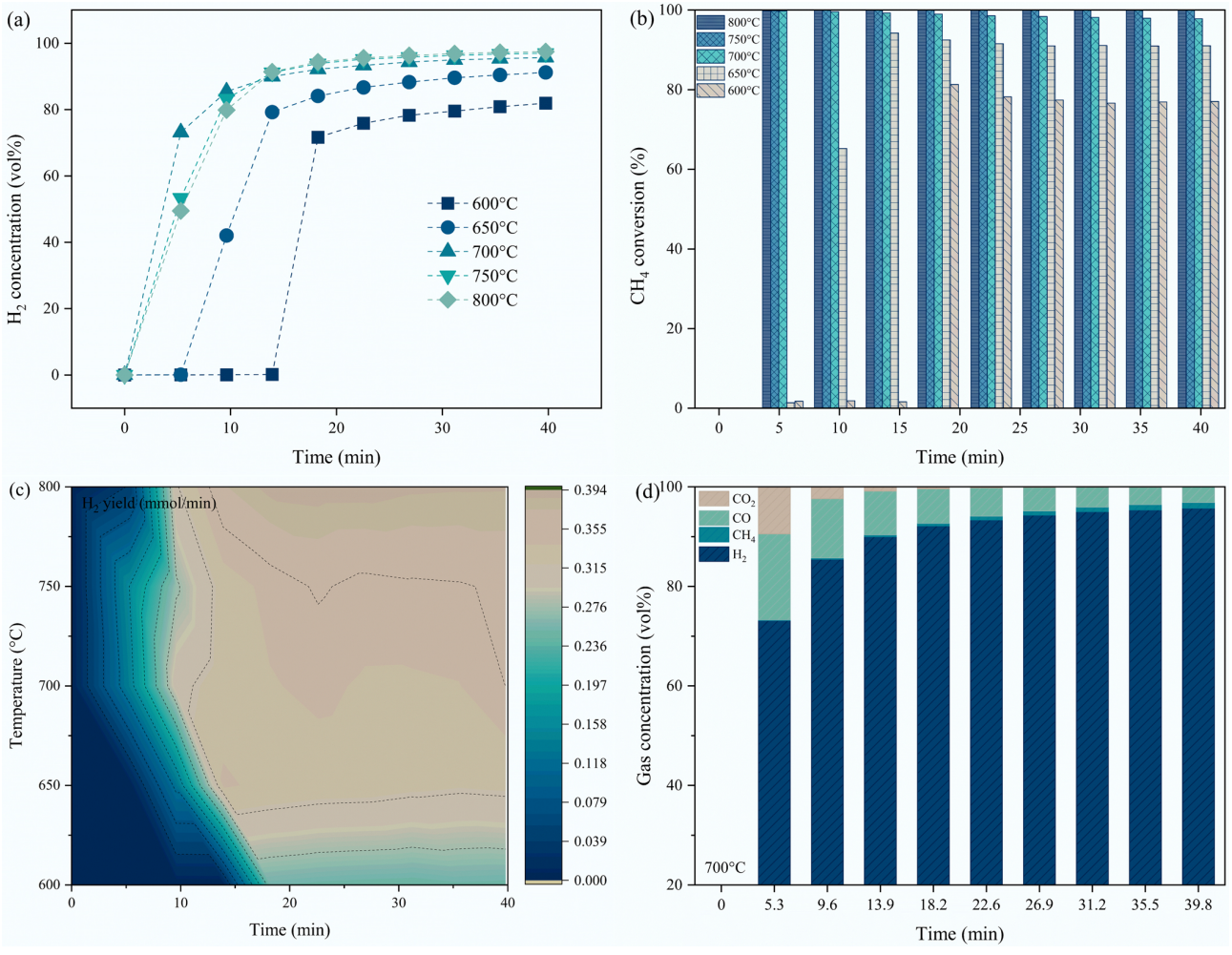

Fig. 6 Effect of methane decomposition temperatures on (**a**) H_2 concentration; (**b**) CH_4 conversion; (**c**) H_2 yield using S3 sample; (**d**) the gas concentrations of H_2, CH_4, CO, CO_2 under S3 catalyst at 700 °C.

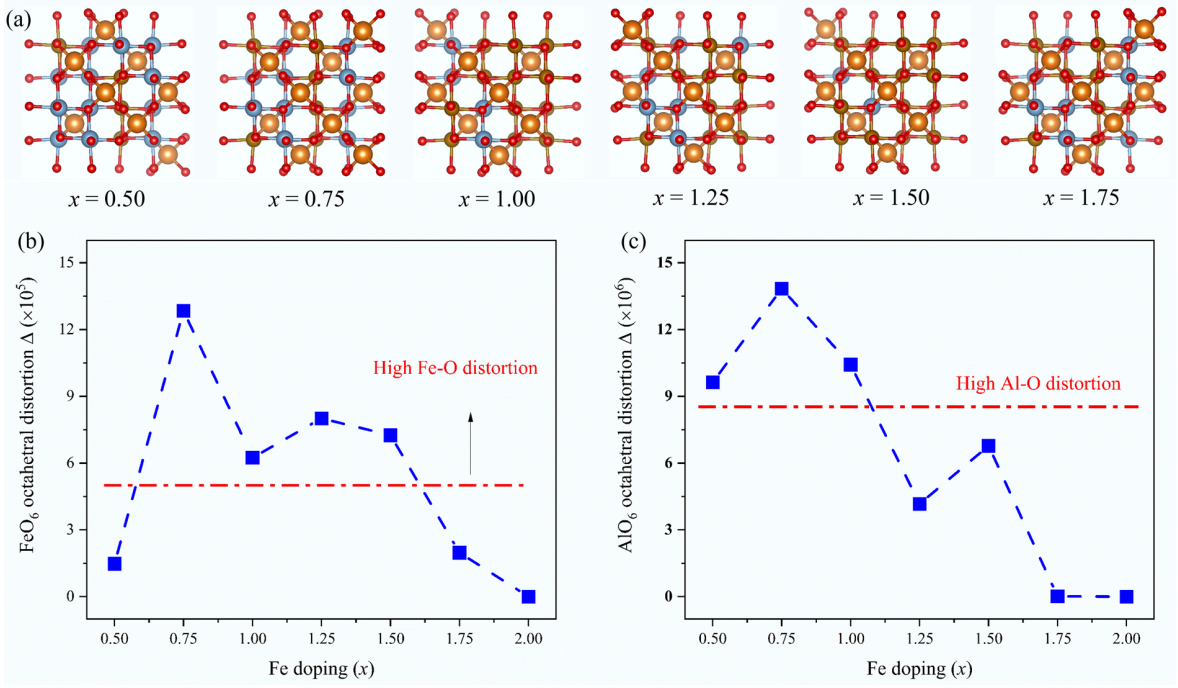

Fig. 7 Lattice distortion analysis: (**a**) bond structure of $MgAl_{2-x}Fe_xO_4$, x = 0.50, 0.75, 1.00, 1.25, 1.50, and 1.75, corresponding to $MgAl_{1.50}Fe_{0.50}O_4$, $MgAl_{1.25}Fe_{0.75}O_4$, $MgAl_{1.00}Fe_{1.00}O_4$, $MgAl_{0.75}Fe_{1.25}O_4$, $MgAl_{0.50}Fe_{1.50}O_4$, and $MgAl_{0.25}Fe_{1.75}O_4$, respectively; (**b**) Fe(Al)O_6 octahedral distortion as a function of Fe doping.

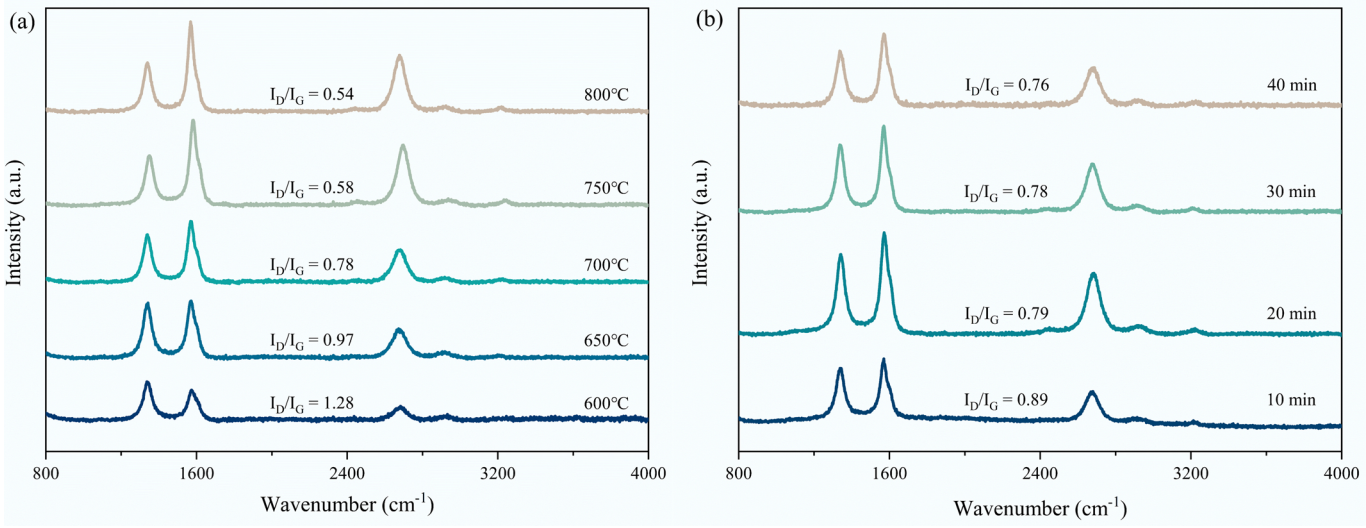

Fig. 8 Raman spectra of (**a**) spent S3 sample after 40 min CMD at 600–800 °C; (**b**) spent S3 sample after 10–40 min CMD at 700 °C.

could be attributed to the *in situ* formation of Ni-Fe alloy as well as the re-generation of $Ni/Mg_2Al_{2-x}Fe_xO_4$ at the CO_2 reduction stage. This phase segregation and re-organization suppresses the particle sintering and agglomeration, thus remaining significant durability under high temperature and carbon deposition conditions. At the initial period of methane decomposition, the phase NiO in the S3 catalyst was reduced and combined with Fe segregated from the support to form a Ni-Fe alloy, which realized efficient dissociation of methane. During the carbon dioxide reduction stage, the Ni-Fe alloy was disassembled. The formation and disassembly of the Ni-Fe alloy promoted the dispersion of Ni and inhibited the sintering and agglomeration of the catalyst to a certain extent. However, by counting the start-up time of the S3 catalyst during 20 cycles, we found that the time required for efficient methane decomposition for hydrogen production gradually increased with the cycle numbers, which can be accounted for by the following reasons: (1) Fe segregated from Ni-Fe alloy and formed FeO_x species on the catalyst surface after carbon dioxide reduction, covering partial nickel-rich particles, thereby prolonging the time required for Ni-Fe alloy formation[40,44,58]; (2) The particle size of the catalyst gradually increases with cycles, leading to slower consumption of lattice oxygen under methane decomposition conditions. As a result, the time required for Ni-Fe alloy formation increases[42]. Apart from the cyclic performance of the S3 catalyst over 20 methane decomposition-carbon dioxide reduction cycles, its phase evolution during the cycle was investigated, as presented in Fig. 10d. After 20 cycles, the phase components of the

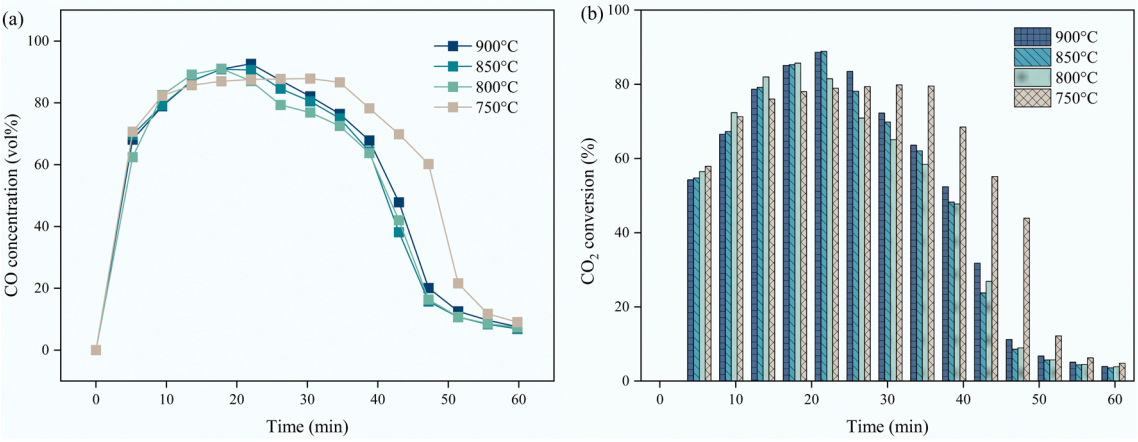

Fig. 9 Effect of carbon dioxide reduction temperatures on the (**a**) CO concentration; (**b**) CO_2 conversion of S3 sample.

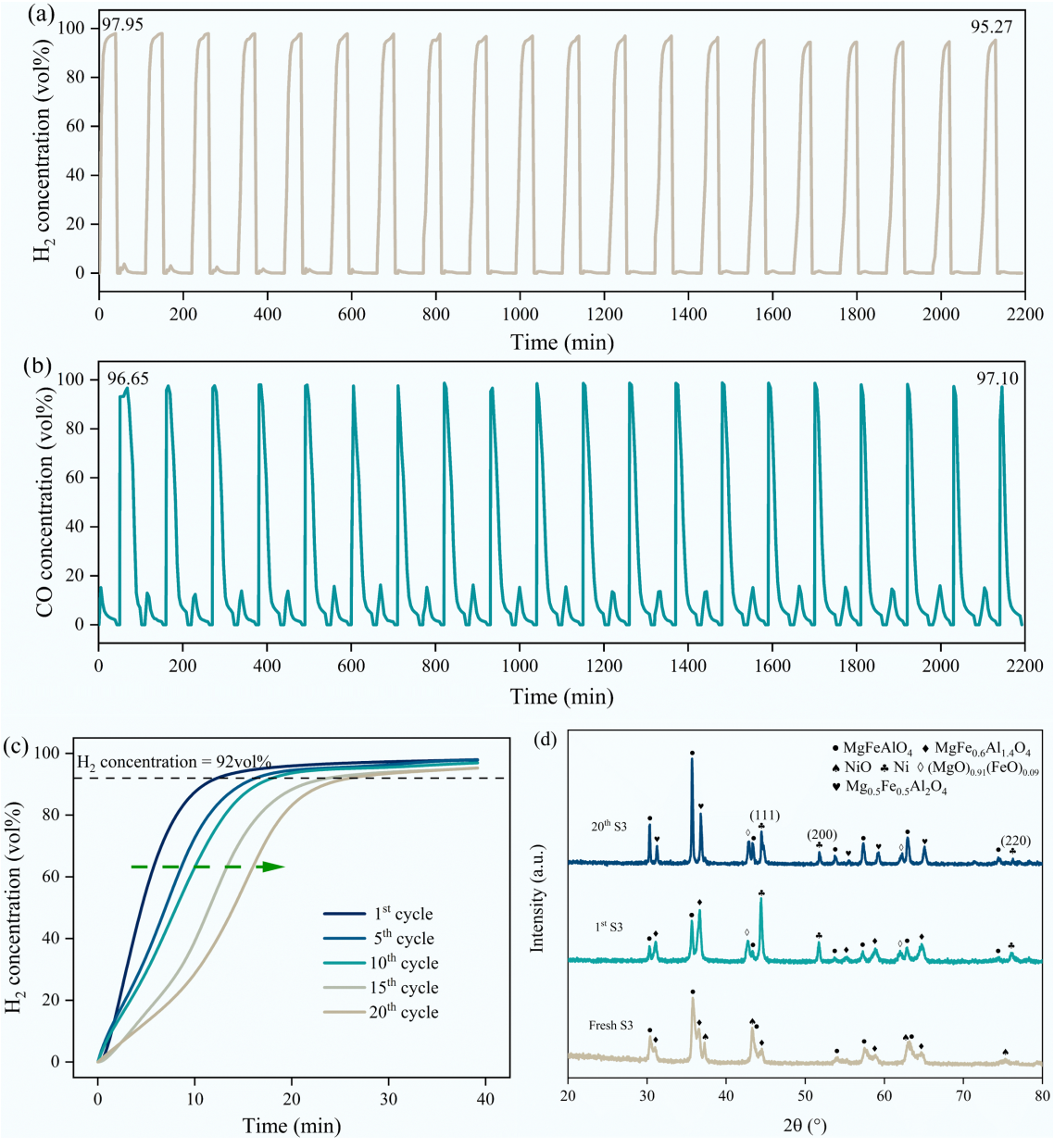

Fig. 10 Cyclic stability test of S3 sample: (**a**) H_2 concentration during 20 cycles; (**b**) CO concentration during 20 cycles; (**c**) Variation of H_2 concentration with time and catalyst activation time in the 1st, 5th, 10th, 15th, and 20th cycles (based on 92 vol% H_2 concentration); (**d**) XRD patterns of significant stages within 20 cycles of reacted S3 sample.

S3 catalyst were basically in line with the 1st cycled state, except that a small proportion of $MgFe_{0.6}Al_{1.4}O_4$ was transformed into $Mg_{0.5}Fe_{0.5}Al_2O_4$. This clarifies the slower lattice oxygen migration rate of the cyclic S3 sample, i.e., the B-site Fe in $MgFe_xAl_{2-x}O_4$ was migrated into the A-site $Mg_xFe_{1-x}Al_2O_4$, thus lowering the lattice oxygen mobility.

To observe the microscopic morphology and element distribution of S3, TEM-EDS was performed on the fresh, 1st cycled, and 20th cycled samples (Supplementary Fig. S5). Fresh samples were made of stacked nanosheets with grooves, while the groove morphology disappeared after one CH_4 decomposition and carbon dioxide reduction cycle, confirming the occurrence of phase segregation and re-organization. EDS mapping results demonstrated that the Ni, Fe, and Al elements of fresh and 1st cycled S3 samples were homogeneously distributed. After 20 cycles, partial Ni, Fe, and Al elements were found to be separated from each other. This indicates that some phases did not undergo recombination, possibly due to incomplete removal of the deposited carbon, which leads to phase isolation.

Conclusion

A series of novel Fe-doped nanostructured supports, $MgAl_{2-x}Fe_xO_4$, were prepared by a sol-gel method, and impregnated with Ni to form an $NiO{\cdot}MgAl_{2-x}Fe_xO_4$ catalyst. The effects of Fe doping, as well as other influencing parameters, on the reactivity and stability of the catalyst and the CMD performance were investigated. Results showed that a proper quantity of Fe doping showed a favorable impact on the improvement of the catalyst performance. Among the synthesized catalysts, $Ni/MgAlFeO_4$ demonstrated the highest catalytic activity, achieving a 97 vol% H_2 concentration and a 100% methane conversion at 750 °C with the generation of deposited carbon with relatively low graphitization degree. Additionally, the catalyst showed satisfactory stability over 20 methane decomposition and carbon dioxide reduction cycles, with only a slight decrease in H_2 concentration observed. This splendid performance is owing to the formation high dispersed Ni-Fe alloy with the induction of Al-O and Fe-O bond distortion. In a typical cycle, the catalyst evolves from $NiO{\cdot}MgFeAlO_4$ to Ni-Fe alloy with $MgFe_{0.6}Al_{1.4}O_4$ and to Ni with $MgFeAlO_4$, demonstrating the occurrence of phase segregation and recombination. Moreover, the inhibition of Ni-Fe phase segregation/reconstruction and the slowing down of lattice oxygen migration rate owing to the phase transformation from $MgFe_xAl_{2-x}O_4$ to $Mg_{0.5}Fe_{0.5}Al_2O_4$ are the dominant factors affecting the multi-cycle activity of catalysts.

Supplementary information

It accompanies this paper at: https://doi.org/10.48130/een-0025-0005.

Authors contributions

The authors confirm their contributions to the paper as follows: study conception and design: All authors; Material preparation, data collection and analysis, draft manuscript preparation: Sun Z, Chen Z; project supervision, manuscript editing: Sun Z. All authors reviewed the results and approved the final version of the manuscript.

Data availability

Datasets generated during and/or analyzed during the current study are available from the corresponding author upon reasonable request.

Funding

This work was supported by the National Key R&D Program of China (2022YFE0206600).

Declarations

Competing interests

The authors declare that they have no conflict of interest.

Author details

Hunan Engineering Research Center of Clean and Low-Carbon Energy Technology, School of Energy Science and Engineering, Central South University, Changsha 410083, China

References

[1] Mazloomi K, Gomes C. 2012. Hydrogen as an energy carrier: Prospects and challenges. *Renewable and Sustainable Energy Reviews* 16:3024–3033

[2] Sartbaeva A, Kuznetsov VL, Wells SA, Edwards PP. 2008. Hydrogen nexus in a sustainable energy future. *Energy & Environmental Science* 1:79–85

[3] Fan Z, Weng W, Zhou J, Gu D, Xiao W. 2021. Catalytic decomposition of methane to produce hydrogen: A review. *Journal of Energy Chemistry* 58:415–430

[4] Bu E, Chen Y, Wang C, Cheng Z, Luo X, et al. 2019. Hydrogen production from bio-derived biphasic photoreforming over a raspberry-like amphiphilic Ag_2O-TiO_2/SiO_2 catalyst. *Chemical Engineering Journal* 370:646–657

[5] Kothari R, Buddhi D, Sawhney RL. 2008. Comparison of environmental and economic aspects of various hydrogen production methods. *Renewable and Sustainable Energy Reviews* 12:553–563

[6] Balat H, Kırtay E. 2010. Hydrogen from biomass – present scenario and future prospects. *International Journal of Hydrogen Energy* 35:7416–7426

[7] Nikolaidis P, Poullikkas A. 2017. A comparative overview of hydrogen production processes. *Renewable and Sustainable Energy Reviews* 67:597–611

[8] Dantas SC, Resende KA, Rossi RL, Assis AJ, Hori CE. 2012. Hydrogen production from oxidative reforming of methane on supported nickel catalysts: an experimental and modeling study. *Chemical Engineering Journal* 197:407–413

[9] Ávila-Neto CN, Dantas SC, Silva FA, Franco TV, Romanielo LL, et al. 2009. Hydrogen production from methane reforming: Thermodynamic assessment and autothermal reactor design. *Journal of Natural Gas Science and Engineering* 1:205–215

[10] Dias JAC, Assaf JM. 2004. Autothermal reforming of methane over Ni/γ-Al_2O_3 catalysts: the enhancement effect of small quantities of noble metals. *Journal of Power Sources* 130:106–110

[11] Chanburanasiri N, Ribeiro AM, Rodrigues AE, Arpornwichanop A, Laosiripojana N, et al. 2011. Hydrogen production via sorption enhanced steam methane reforming process using Ni/CaO multifunctional catalyst. *Industrial & Engineering Chemistry Research* 50:13662–13671

[12] Bakenne A, Nuttall W, Kazantzis N. 2016. Sankey-Diagram-based insights into the hydrogen economy of today. *International Journal of Hydrogen Energy* 41:7744–7753

[13] Upham DC, Agarwal V, Khechfe A, Snodgrass ZR, Gordon MJ, et al. 2017. Catalytic molten metals for the direct conversion of methane to hydrogen and separable carbon. *Science* 358:917–920

[14] Ashok J, Raju G, Reddy PS, Subrahmanyam M, Venugopal A. 2008. Catalytic decomposition of CH_4 over Ni-Al_2O_3-SiO_2 catalysts: Influence of pretreatment conditions for the production of H_2. *Journal of Natural Gas Chemistry* 17:113–119

[15] Pudukudy M, Yaakob Z, Mazuki MZ, Takriff MS, Jahaya SS. 2017. One-pot sol-gel synthesis of MgO nanoparticles supported nickel and iron

catalysts for undiluted methane decomposition into COx free hydrogen and nanocarbon. *Applied Catalysis B: Environmental* 218:298–316

[16] Marquardt T, Bode A, Kabelac S. 2020. Hydrogen production by methane decomposition: analysis of thermodynamic carbon properties and process evaluation. *Energy Conversion and Management* 221:113125

[17] Pudukudy M, Yaakob Z. 2015. Methane decomposition over Ni, Co and Fe based monometallic catalysts supported on sol gel derived SiO_2 microflakes. *Chemical Engineering Journal* 262:1009–1021

[18] Fincke JR, Anderson RP, Hyde TA, Detering BA. 2002. Plasma pyrolysis of methane to hydrogen and carbon black. *Industrial & Engineering Chemistry Research* 41:1425–1435

[19] Chen Z, Zhang R, Xia G, Wu Y, Li H, et al. 2021. Vacuum promoted methane decomposition for hydrogen production with carbon separation: Parameter optimization and economic assessment. *Energy* 222:119953

[20] Liang W, Yan H, Feng X, Chen C, Lin D, et al. 2020. NiMgAlMo catalyst derived from a guest-host MoO_4^{2-} mediated layered double hydroxide: High performance for the methane decomposition reaction. *Applied Catalysis A: General* 597:117551

[21] Ashik UPM, Wan Daud WMA, Abbas HF. 2015. Production of greenhouse gas free hydrogen by thermocatalytic decomposition of methane – a review. *Renewable and Sustainable Energy Reviews* 44:221–256

[22] Tajuddin MM, Ideris A, Ismail M. 2019. In situ glycine-nitrate combustion synthesis of Ni-La/SiO_2 catalyst for methane cracking. *Industrial & Engineering Chemistry Research* 58:531–538

[23] Sikander U, Samsudin MF, Sufian S, KuShaari K, Kait CF, et al. 2019. Tailored hydrotalcite-based Mg-Ni-Al catalyst for hydrogen production via methane decomposition: effect of nickel concentration and spinel-like structures. *International Journal of Hydrogen Energy* 44:14424–14433

[24] Li Y, Li D, Wang G. 2011. Methane decomposition to CO_x-free hydrogen and nano-carbon material on group 8–10 base metal catalysts: a review. *Catalysis Today* 162:1–48

[25] Farooqi AS, Yusuf M, Mohd Zabidi NA, Saidur R, Sanaullah K, et al. 2021. A comprehensive review on improving the production of rich-hydrogen via combined steam and CO_2 reforming of methane over Ni-based catalysts. *International Journal of Hydrogen Energy* 46:31024–31040

[26] Rahmat N, Yaakob Z, Mat Hassan NS. 2021. Hydrogen rich syngas from CO_2 reforming of methane with steam catalysed by facile fusion-impregnation of iron and cobalt loaded $MgAl_2O_4$ catalyst with minimal carbon deposits. *Journal of the Energy Institute* 96:61–74

[27] Ganesh I. 2013. A review on magnesium aluminate ($MgAl_2O_4$) spinel: synthesis, processing and applications. *International Materials Reviews* 58:63–112

[28] Nuernberg GDB, Foletto EL, Campos CEM, Fajardo HV, Carreño NLV, et al. 2012. Direct decomposition of methane over Ni catalyst supported in magnesium aluminate. *Journal of Power Sources* 208:409–414

[29] Yu S, Hu Y, Cui H, Cheng Z, Zhou Z. 2021. Ni-based catalysts supported on $MgAl_2O_4$ with different properties for combined steam and CO_2 reforming of methane. *Chemical Engineering Science* 232:116379

[30] Jaiswar VK, Katheria S, Deo G, Kunzru D. 2017. Effect of Pt doping on activity and stability of Ni/$MgAl_2O_4$ catalyst for steam reforming of methane at ambient and high pressure condition. *International Journal of Hydrogen Energy* 42:18968–18976

[31] Li D, Atake I, Shishido T, Oumi Y, Sano T, et al. 2007. Self-regenerative activity of Ni/Mg(Al)O catalysts with trace Ru during daily start-up and shut-down operation of CH_4 steam reforming. *Journal of Catalysis* 250:299–312

[32] Takenaka S, Shigeta Y, Tanabe E, Otsuka K. 2003. Methane decomposition into hydrogen and carbon nanofibers over supported Pd-Ni catalysts. *Journal of Catalysis* 220:468–477

[33] Torres D, Pinilla JL, Suelves I. 2018. CO-, Cu- and Fe-doped Ni/Al_2O_3 catalysts for the catalytic decomposition of methane into hydrogen and carbon nanofibers. *Catalysts* 8:300

[34] Ayillath Kutteri D, Wang IW, Samanta A, Li L, Hu J. 2018. Methane decomposition to tip and base grown carbon nanotubes and CO_x-free H_2 over mono- and bimetallic 3d transition metal catalysts. *Catalysis Science & Technology* 8:858–869

[35] Sun Z, Gong Y, Cheng D, Sun Z. 2024. Reinforcing hydrogen and carbon nanotube co-production via Cr–O–Ni catalyzed methane decomposition. *Journal of Materials Chemistry A* 12:4893–4902

[36] Sun Z, Russell CK, Whitty KJ, Eddings EG, Dai J, et al. 2023. Chemical looping-based energy transformation via lattice oxygen modulated selective oxidation. *Progress in Energy and Combustion Science* 96:101045

[37] Chesnokov VV, Chichkan AS. 2009. Production of hydrogen by methane catalytic decomposition over Ni-Cu-Fe/Al_2O_3 catalyst. *International Journal of Hydrogen Energy* 34:2979–2985

[38] Bayat N, Rezaei M, Meshkani F. 2016. Methane decomposition over Ni–Fe/Al_2O_3 catalysts for production of CO_x-free hydrogen and carbon nanofiber. *International Journal of Hydrogen Energy* 41:1574–1584

[39] Muraza O, Galadima A. 2015. A review on coke management during dry reforming of methane. *International Journal of Energy Research* 39:1196–1216

[40] Theofanidis SA, Galvita VV, Sabbe M, Poelman H, Detavernier C, et al. 2017. Controlling the stability of a Fe-Ni reforming catalyst: structural organization of the active components. *Applied Catalysis B: Environmental* 209:405–416

[41] Sun Z, Chen S, Hu J, Chen A, Rony AH, et al. 2018. Ca_2Fe2O_5: a promising oxygen carrier for CO/CH_4 conversion and almost-pure H_2 production with inherent CO_2 capture over a two-step chemical looping hydrogen generation process. *Applied Energy* 211:431–442

[42] Sun Z, Cai T, Russell CK, Johnson JK, Ye RP, et al. 2020. Highly efficient methane decomposition to H_2 and CO_2 reduction to CO via redox looping of $Ca_2FexAl_{2-x}O_5$ supported $NiyFe_{3-y}O_4$ nanoparticles. *Applied Catalysis B: Environmental* 271:118938

[43] Azancot L, Bobadilla LF, Centeno MA, Odriozola JA. 2021. Effect of potassium loading on basic properties ofNi/$MgAl_2O_4$ catalyst for CO_2 reforming of methane. *Journal of CO_2 Utilization* 52:101681

[44] Theofanidis SA, Galvita VV, Poelman H, Dharanipragada NVRA, Longo A, et al. 2018. Fe-containing magnesium aluminate support for stability and carbon control during methane reforming. *ACS Catalysis* 8:5983–5995

[45] Dharanipragada NVRA, Buelens LC, Poelman H, De Grave E, Galvita VV, et al. 2015. Mg-Fe-Al-O for advanced CO_2 to CO conversion: carbon monoxide yield vs. *oxygen storage capacity. Journal of Materials Chemistry A* 3:16251–16262

[46] Ortega KF, Rein D, Lüttmann C, Heese J, Özcan F, et al. 2017. Ammonia decomposition and synthesis over multinary magnesioferrites: Promotional effect of Ga on Fe catalysts for the decomposition reaction. *Chemcatchem* 9:659–671

[47] Kumar GM, Cho HD, Lee DJ, Kumar JR, Siva C, et al. 2021. Elevating the charge separation of $MgFe_2O_4$ nanostructures by Zn ions for enhanced photocatalytic and photoelectrochemical water splitting. *Chemosphere* 283:131134

[48] Zhang M, Yu F, Li J, Chen K, Yao Y, et al. 2018. High CO methanation performance of two-dimensional Ni/MgAl layered double oxide with enhanced oxygen vacancies via flash nanoprecipitation. *Catalysts* 8:363

[49] Rastegarpanah A, Rezaei M, Meshkani F, Zhang K, Zhao X, et al. 2019. Influence of group VIB metals on activity of the Ni/MgO catalysts for methane decomposition. *Applied Catalysis B: Environmental* 248:515–525

[50] Qian JX, Liu DB, Basset JM, Zhou L. 2021. Methane decomposition to produce hydrogen and carbon nanomaterials over costless, iron-containing catalysts. *Journal of Cleaner Production* 320:128879

[51] Kim H, Eissa AA-S, Kim SB, Lee H, Kim W, et al. 2021. One-pot synthesis of a highly mesoporous Ni/$MgAl_2O_4$ spinel catalyst for efficient steam methane reforming: influence of inert annealing. *Catalysis Science & Technology* 11:4447–4458

[52] Jabbour K, Massiani P, Davidson A, Casale S, El Hassan N. 2017. Ordered mesoporous "one-pot" synthesized Ni-Mg(Ca)-Al_2O_3 as effective and remarkably stable catalysts for combined steam and dry

reforming of methane (CSDRM). *Applied Catalysis B: Environmental* 201:527–542

[53] Rastegarpanah A, Meshkani F, Rezaei M. 2017. Thermocatalytic decomposition of methane over mesoporous nanocrystalline promoted Ni/MgO·Al_2O_3 catalysts. *International Journal of Hydrogen Energy* 42:16476–16488

[54] Yu Y, Cui M, Li M, Zhao N, Long Z, et al. 2014. Rare earth modified Ni-Si catalysts for hydrogen production from methane decomposition. *Journal of Rare Earths* 32:709–714

[55] Zhang J, Ren M, Li X, Hao Q, Chen H, et al. 2020. Ni-based catalysts prepared for CO_2 reforming and decomposition of methane. *Energy Conversion and Management* 205:112419

[56] Ashok J, Kawi S. 2014. Nickel-iron alloy supported over iron-alumina catalysts for steam reforming of biomass tar model compound. *ACS Catalysis* 4:289–301

[57] Theofanidis SA, Galvita VV, Poelman H, Marin GB. 2015. Enhanced carbon-resistant dry reforming Fe-Ni catalyst: Role of Fe. *ACS Catalysis* 5:3028–3039

[58] Kim SM, Abdala PM, Margossian T, Hosseini D, Foppa L, et al. 2017. Cooperativity and dynamics increase the performance of NiFe dry reforming catalysts. *Journal of the American Chemical Society* 139:1937–1949

[59] Zhang X, Pei C, Chang X, Chen S, Liu R, et al. 2020. FeO_6 octahedral distortion activates lattice oxygen in perovskite ferrite for methane partial oxidation coupled with CO_2 splitting. *Journal of the American Chemical Society* 142:11540–11549

[60] Shannon RD. 1976. Revised effective ionic radii and systematic studies of interatomic distances in halides and chalcogenides. *Acta Crystallographica Section A: Foundations and Advances* A32:751–767

[61] Hirata T. 2000. Oxygen Position, Octahedral Distortion, and Bond-Valence Parameter from Bond Lengths in $Ti_{1-x}Sn_xO_2$ ($0 \le x \le 1$). *Journal of the American Ceramic Society* 83:3205–3207